

A local-scale, high-resolution evapotranspiration mapping algorithm (ETMA) with hydroecological applications at riparian meadow restoration sites

Steven P. Loheide II*, Steven M. Gorelick

Department of Geological and Earth Sciences, Stanford University, Stanford, CA 94305-2115, USA

Received 10 March 2005; received in revised form 24 June 2005; accepted 2 July 2005

Abstract

We present a new algorithm for mapping evapotranspiration (ET) that requires only local weather-station data including the ground heat flux and high resolution airborne thermal imagery. This ET mapping algorithm (ETMA) is based on the surface energy budget and partitions the available energy between the latent and sensible heat fluxes. Two parameters T_{latent} and T_{sensible} are defined as the surface temperatures at which all of the turbulent heat flux is accounted for by the latent and sensible heat fluxes, respectively. These points are used to develop linear relationships between surface temperature and ET at specified times. Maps of ET at two times during the day are then used to model and integrate the diurnal pattern of ET using the Penman–Montieth and Jarvis–Stewart models of ET and surface resistance. The resulting maps of daily integrated ET have 1-m spatial resolution that is rarely available, yet important to the fields of hydrology, ecology, forestry, and agriculture. Our results comparing ET values to porometry-based local measurements within the meadows suggest that the mapped ET_{day} values are accurate to within 10% of the potential ET rate or within 0.7 mm absolute error; however, under different conditions the error may be larger. The purpose of developing this algorithm was to investigate the hydroecology of restored and degraded meadows in the Sierra Nevada of northern California, USA. The pond-and-plug method of riparian restoration aims to raise the water table and re-establish native mesic vegetation that has been replaced by sagebrush and dryland species due to land-use practices over the past 150 years. By comparing the ET regime of two restored and two degraded meadows, we show that daily ET in the restored meadows (5–6.5 mm/day) was approximately twice that of the degraded ones (1.5–4 mm/day). The detailed images of ET show local impacts of land-use change and re-vegetation efforts. © 2005 Elsevier Inc. All rights reserved.

Keywords: Evapotranspiration; Hydroecology; Riparian restoration; Pond-and-plug method; High-resolution; Thermal imagery; Meadow

1. Introduction

Evapotranspiration (ET) is a critical component of the hydrologic budget and measurements are needed in the fields of hydrology, ecology, forestry, meteorology, and agriculture. Spatially distributed point measurements of ET are time consuming to obtain, may not be representative, and are difficult to upscale spatially. Remote sensing has been used to estimate the spatial distribution of ET because it is the only means by which regional and global trends can

be obtained economically (Bastiaanssen et al., 1998; Boegh et al., 2002; Carlson et al., 1995; Goodrich et al., 2000; Granger, 2000; Kite & Droogers, 2000; Kustas & Norman, 1996; Nagler et al., 2005; Pietroniro & Prowse, 2002; Qiu et al., 2002; Schultz & Engman, 2000; and many others). Satellite-based methods for mapping ET have proven to be very useful for regional and global scale estimation of ET, particularly in regard to global climate models. However, satellite images do not provide the meter-scale resolution desired for many applications such as ecosystem restoration and precision agriculture, and the coarse resolution introduces significant error due to subpixel heterogeneity (Kustas & Norman, 2000). The SEBAL algorithm (Bastiaanssen et al., 1998) in particular has seen wide application using

* Corresponding author.

E-mail addresses: sloheide@stanford.edu (S.P. Loheide), gorelick@geo.stanford.edu (S.M. Gorelick).

satellite data (e.g., Bastiaanssen et al., 2002) and a variant has also been applied and validated using airborne data with 20 m spatial resolution (Jacob et al., 2002). Moran (2003) recognized the value of high-resolution thermal imagery as an indicator of plant ecosystem health and Norman et al. (2003) developed an algorithm for routine estimation of surface energy fluxes including ET at the 10–100 m scale. In this work, we take advantage of a relatively low cost forward-looking infrared (FLIR) camera to obtain very high resolution (1-m) thermal imagery, which is advantageous for four reasons: 1) there is a reduction of uncertainty introduced by subpixel mixing; 2) limitation to a local scale improves the assumption that meteorological variables can be measured on site and have a high degree of spatial uniformity; 3) differences between single- or dual-source and mosaic patch models become smaller as pixel size approaches the scale of heterogeneity (Boulet et al., 1998; Lhomme & Chehbouni, 1999); and 4) detailed variation in ET patterns that would be lost with coarser resolution can be observed and can help provide an understanding of the process, distribution, and nature of ET. The objectives of this research are to develop a cost effective and transferable methodology for mapping site-scale, daily ET at a very high spatial resolution and to apply it in a comparative analysis of restored and degraded mountain meadows.

Our work builds on the well-established approach first demonstrated by Jackson et al. (1977) in which ET is assumed to be linearly related to the difference between the air temperature and the leaf temperature. A formal theoretical treatment of ET estimation by remote sensing of surface temperature was given by Gash (1987). In an approach related to that of Suleiman and Crago (2004), we use the surface energy budget to obtain a linear relationship between surface temperature and instantaneous ET (ET_{inst}). In both our approach and that of Suleiman and Crago (2004), the latent and sensible heat fluxes are partitioned based on derived surface temperatures associated with zero ET and potential ET rates. Although more complicated approaches such as the multilayer and patch models are available (Caurault et al., 2003; Kustas et al., 1996; Lhomme & Chehbouni, 1999), we choose to use the simplified approach in part because the averaging and pixel mixing is minimized by our high-resolution imagery that is similar to the scale of the spatial variability of the vegetation at the site.

In the past, instantaneous values obtained in the simplified case were extended to daily values (ET_{day}) by Nieuwenhuis et al. (1985) and Seguin and Itier (1983). Two key assumptions often used in the analysis of ET_{day} have been compared by Zhang and Lemeur (1995). One assumption is based on Jackson et al. (1983) who showed that the ratio of midday solar radiation to daily solar radiation can be predicted for clear-day conditions and others have assumed that this ratio was equivalent to that of the midday to daily latent heat flux (Brutsaert & Sugita, 1992). The second assumption, which is supported by

observations by Hall et al. (1992) and modeling by Lhomme and Elguero (1999), is that the evaporative fraction is constant during the day, a fact that has led many to scale instantaneous values to daily values using estimates of the evaporative fraction and the daily available energy. Although both assumptions appear to be valid under certain conditions, in this study, we rely on neither assumption but instead use the Penman–Monteith ET equation and the Jarvis–Stewart stomatal response model to simulate the diurnal pattern of ET at each pixel location.

The local-scale ET mapping algorithm (ETMA) presented here is based on the linkage between the water and energy budgets. Airborne thermal imagery and weather station data including the ground heat flux are required. Maps of surface temperature collected at two times during daylight hours are used to partition energy between the latent and sensible heat fluxes. Meteorological data are used to estimate the available energy and to model the daily pattern of ET. Using the two estimates of ET_{inst} at each pixel location, a best fit model of ET for that day is found by varying the surface resistance. Given this best fit daily pattern, ET_{day} is determined by integration of ET_{inst} values over the entire day.

2. Site background

2.1. Riparian ecosystem restoration

The majority of riparian areas in the USA have been degraded or converted for urban or agricultural use (WSTB, 2002). The value of restoring these lands has been widely recognized and the San Francisco Bay-Delta Watershed in California, USA is no exception. From 2000–2004, the CALFED program spent over 2 billion dollars within the San Francisco Bay-Delta Watershed with the goal of preserving and restoring the ecosystem (NEMW, 2005); however, this is likely a small percentage of future costs. We studied the Last Chance Watershed (Fig. 1) in the headwaters of this large-scale restoration initiative. The Last Chance Watershed occupies 250 km² in the northern Sierra Nevada in Plumas National Forest, CA, approximately 100 km northwest of Reno, NV.

The Last Chance Watershed is a semi-arid mountain environment at elevations ranging from 1675 to 2250 m and contains the longest contiguous meadow system (60 km) in the Sierra Nevada. The meadow system is our focus, as it plays a critical role linking the hydrology to the flora, fauna, and all aspects of the ecosystem in the Sierra Nevada (Ratliff, 1985). The hydrology of Last Chance Watershed is snowmelt-driven with most of the precipitation occurring from November through March and an annual dry period occurring during the summer. Under pristine conditions (Fig. 2A), the wet meadows are vegetated with hydric and mesic species such as sedges (*Carex spp.*), rushes (*Juncus*

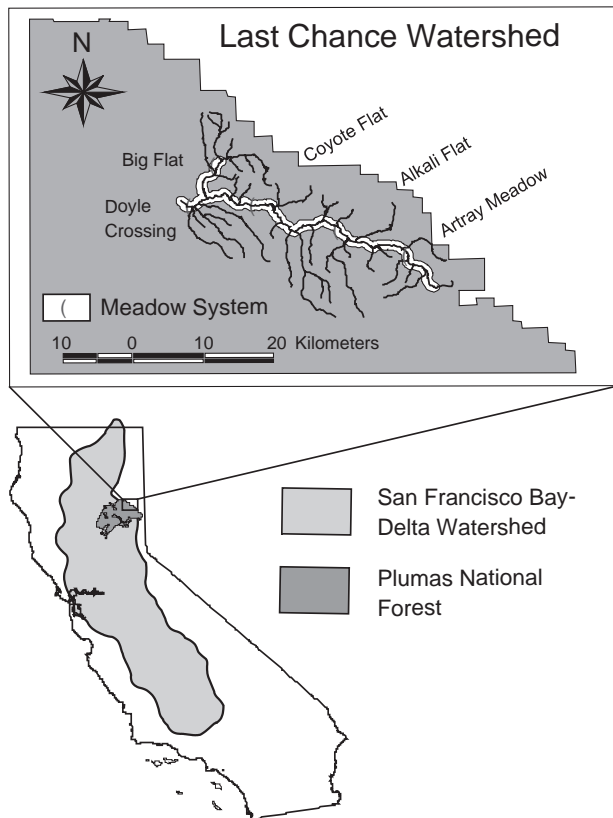


Fig. 1. Map showing location of study meadows within the Last Chance Watershed. The map also shows the location of this watershed within Plumas National Forest and the San Francisco Bay-Delta Watershed, which is the focus of the large-scale restoration initiative headed by CALFED Bay-Delta Authority.

spp.), and other herbaceous species. Xeric vegetation communities such as the sagebrush scrub (i.e., *Artemisia tridentata*, *Purshia tridentata*—antelope bitterbrush, and *Chrysothamnus nauseosus*—rabbitbrush) and yellow pine/juniper (i.e., *Pinus jeffreyi*, *Pinus ponderosa*, and *Juniperus occidentalis* var. *australis*) dominate on the hillslopes. Under historic pristine conditions, the meadow system played a buffering role in the hydrology of these mountainous regions. Rosgen “E” type streams (Rosgen, 1996) meandered through the meadows, flooding extensively during the snowmelt season particularly during rain-on-snow events. These spring floods infiltrate the meadow sediments and wet meadow vegetation depends on the shallow groundwater for survival through the annual dry summer period. The meadow systems are groundwater-dependent ecosystems as defined by Murray et al. (2003) because they require a shallow groundwater table to maintain their current composition and functioning.

Unfortunately, almost all of the riparian meadows of Last Chance Watershed have been degraded during the past 140 years by land-use practices (Lindquist & Wilcox, 2000). The degradation is tied to incision of the channel as shown in Fig. 2B that was likely initiated by human activities such as livestock grazing, logging, and railroad/road construction.

The incision is up to 6 m in some stream reaches and has resulted in a lowering of the water table. As the water table dropped below the root zone, a succession occurred from meadow mesic species to xeric vegetation such as sagebrush and dryland grasses. This change in vegetation has resulted in decreased root strength (Micheli & Kirchner, 2002), which in turn promotes accelerated erosion. This cycle continues in a positive feedback loop that has negative environmental consequences and reduces the productivity of the land.

Persistent deterioration in Last Chance Creek and the larger Feather River Watershed led to the establishment in 1985 of the Feather River Coordinated Resource Management Group (FRCRM), which is a non-profit partnership of 23 public and private watershed stakeholders (FRCRM, 1997). The FRCRM is pioneering the pond-and-plug restoration technique in California. This technique involves obliterating the incised channel using heavy machinery and reactivating or establishing a new shallow channel (Fig. 2C). The aim is to restore a more natural hydrologic and ecologic meadow function.

The first step of pond-and-plug restoration is selecting a reach where streamflow can be diverted into a new channel. The approach attempts to reactivate remnant, abandoned, Rosgen type “E” channels because they have naturally stable width, depth, slope, and sinuosity for the meadow environment and are in equilibrium with established vegetation that in turn helps ensure channel stability. Some segments of the new channel may be created and a control structure is often required to return the stream to the incised channel at the downstream end where an adjacent degraded meadow exists. After the new channel is prepared, the second step is to reroute the water into the new channel by creating an upstream plug that prevents flow to the old channel. Some boulders and rip-rap are transported to the site, but most of the plug material is obtained by excavation near the incised channel. The old, incised channel is replaced with a series of excavated ponds that mimic oxbow lakes and are separated by plugs. Establishing new shallow channels causes the water table to rise within 1 to 2 seasons. This rise causes an increase in soil moisture in the root zone and waterlogging of the meadow which kills the sagebrush and other dryland vegetation. The moister conditions initiate the succession of native wet meadow vegetation. Re-vegetation is further enhanced by various means. First, the topsoil is stored and later spread on the newly created plugs to provide a viable seed bank. Second, at some sites, native seeds are manually harvested and dispersed on the plugs to encourage new vegetation growth. Third, efforts are made to transplant any healthy sod mats or willows that were growing near the degraded channel.

The restored meadows experience not only a rise in the water table and a return of native meadow vegetation but also a flood regime reminiscent of pristine conditions. The meadows flood annually during the spring, recharging the

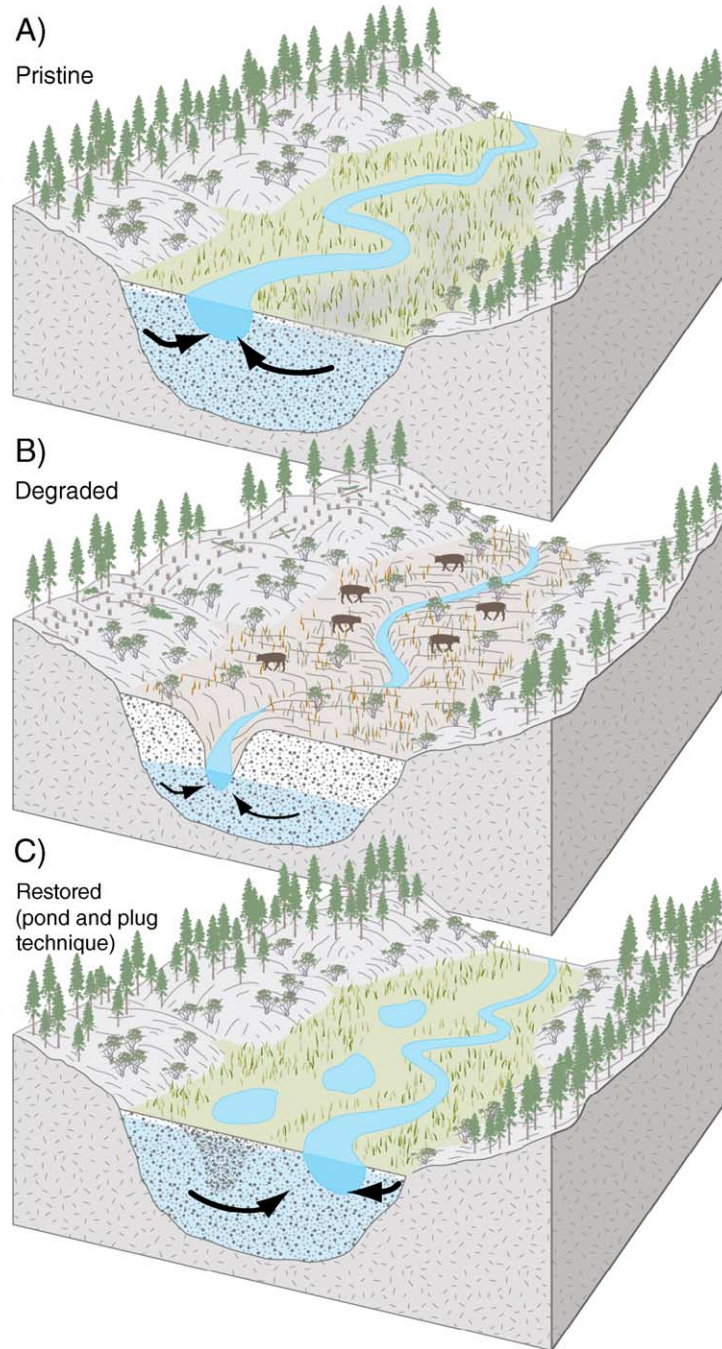


Fig. 2. Conceptual model of pristine, degraded, and restored meadow function. A) Pristine case with meandering channel, a shallow water table, and meadow vegetation. B) Degraded case resulting from land-use practices such as over-grazing and logging with a deeply incised channel, dewatered meadow sediments, and a change to a sagebrush scrub vegetation community. C) Restored case in which the pond-and-plug technique has been applied to raise the water table and encourage the return of rushes, sedges, and other native meadow vegetation.

meadow sediments and temporarily storing water on the meadow surface, both of which decrease the magnitude of the flood pulse downstream. It has been presumed that after restoration, groundwater stored in a meadow's unconfined aquifer is released as baseflow to the stream during the dry summer season. This is desirable because it increases minimum streamflows which, in turn, improves the aquatic habitat, reduces stream temperature, and increases water

availability at downstream reservoirs during the summer when demand is highest. However, in order to determine whether late season baseflow is in fact increased, the annual water budget must be closed. In this paper we propose a method to accurately map ET in meadow or other riparian environments. This information is essential to quantify the effects of restoration on subsurface water storage and baseflow production.

2.2. Meadow descriptions

We develop ET maps and compare ET regimes for two restored and two degraded meadows, three of which are on public lands in Plumas National Forest and one of which is privately owned. Here the site history of each meadow is described. At an elevation of 1701 m, Coyote Flat is the most severely degraded meadow with a channel that is incised up to 5 m exposing a hard, lacustrine clay that overlies the volcanic bedrock. The steep, unvegetated, silty channel banks are unstable and continue to erode although grazing along the channel has been discontinued. The site is dominated by sagebrush and dryland vegetation (i.e., *Artemisia tridentata*, *Poa secunda* ssp. *secunda*, and *Hordeum jubatum*). Several remnant channels at ~1–1.5 m below the meadow serve as refuge areas for meadow species (i.e., *Juncus balticus* and *Carex* spp). The incised channel has begun to develop an inset flood plain at a lower elevation and willows (*Salix* spp.) have established themselves on these poorly developed soils.

The second degraded site is Doyle Crossing, which is at an elevation of 1679 m. A bridge and abutment structure confines flow to the channel at the upper boundary of this site where the stream has incised to the basalt bedrock. In addition, an abandoned railroad bed bisects the floodplain and may be related to initial stream incision. A relatively healthy tributary meadow with high subsurface flow, but infrequent surface flow, enters Last Chance Creek at this site. The tributary meadow is lushly vegetated with a diverse mixture of sedges, rushes, and other wetland/herbaceous species. Most of the soil has been stripped from the north side of the stream, which is now occupied by willow (*Salix* spp.). In the degraded portions of the flood plain south of an abandoned railroad bed, the soil remains, but sagebrush has replaced the meadow vegetation.

Alkali Flat is a meadow at an elevation of 1745 m that was restored in July 2003 with pond-and-plug restoration. Prior to restoration, the channel was incised by ~2 m. Gully elimination required the construction of four ponds and movement of 5960 m³ of meadow sediments (Plumas Corporation, 2004). In spring 2004, portions of the meadow flooded during snowmelt. Last Chance Creek is intermittent in this reach. From August 2003 through June 2004, much of the sagebrush died from waterlogged conditions and meadow vegetation re-established itself. Vegetation on the plugs did not flourish until mid-summer 2004. Grazing was not allowed near the newly created ponds during 2004.

Artray Meadow is situated at an elevation of 1813 m and was restored during fall 2002 using the pond-and-plug technique that required moving 5250 m³ of sediment and the creation of seven ponds (Plumas Corporation, 2004). During spring flooding, water flows diffusely over the meadow and the ponds overflow their banks. This headwater meadow has a relatively small area contributing to runoff; thus, late summer surface flows are rare. Meadow vegetation is

strongly established across this meadow with high species diversity, but vegetation is not as lush on the 7300 m² of plug area.

3. Methods

3.1. Data collection

3.1.1. Thermal imagery

We collected high resolution thermal imagery of the riparian zone along Last Chance Creek.¹ Two sets of snapshot images were collected on June 3, 2004, from 12:35–12:59 and 4:29–5:10 PM, and will hereafter be referred to as the 12:45 and 5:00 flights, respectively. A forward-looking infrared (FLIR) camera² was mounted beneath a helicopter adjacent to the open door frame and was maintained in a near vertical orientation (<10° deviation) with a manually controlled, custom-designed mount. The flight path followed the stream channel at an elevation of 700–940 m above the land surface, which resulted in images whose long side spanned 300–400 m, capturing nearly the entire meadow system at a pixel resolution of 0.93–1.25 m. The camera collected images at a rate of 7.5 Hz as it traveled at an average velocity of 45 m/s resulting in significant overlap in sequential images.

The FLIR camera has a 320 × 240 pixel, uncooled microbolometer, focal plane array detector. An emissivity value must be selected to describe the percentage of radiation emitted from the vegetation to the total amount received by the sensor. Jenson (2000) lists emissivity values for dry soil, wet soil, open canopy, and closed vegetation canopy that range from 0.92 to 0.98. In this application a value of 0.92 was selected. The other radiation detected by the sensor is reflected from the vegetated surface and is represented by the apparent radiometric temperature of the atmosphere, which is the temperature the sensor would record for the atmosphere given the object parameters used by the camera (i.e., emissivity, target distance, and humidity). This quantity was estimated prior to each flight by recording an average value obtained by imaging a portion of the sky directly overhead which does not include the sun. The parameters such as target distance, humidity, and air temperature are used by the FLIR camera to correct for atmospheric attenuation. Instream groundtruth temperature data were collected using instream Hobo temperature loggers³ throughout the day and the mean absolute difference between 67 paired Hobo and FLIR measurements was less than 0.7 °C.

¹ FLIR data were collected under contract by InfraRed Image Solutions, (Hermiston, OR).

² Model number S60 produced by FLIR, (North Billerica, MA).

³ Hobo Water Temp Pro Dataloggers produced by Onset Computer Corp, (Pocasset, MA).

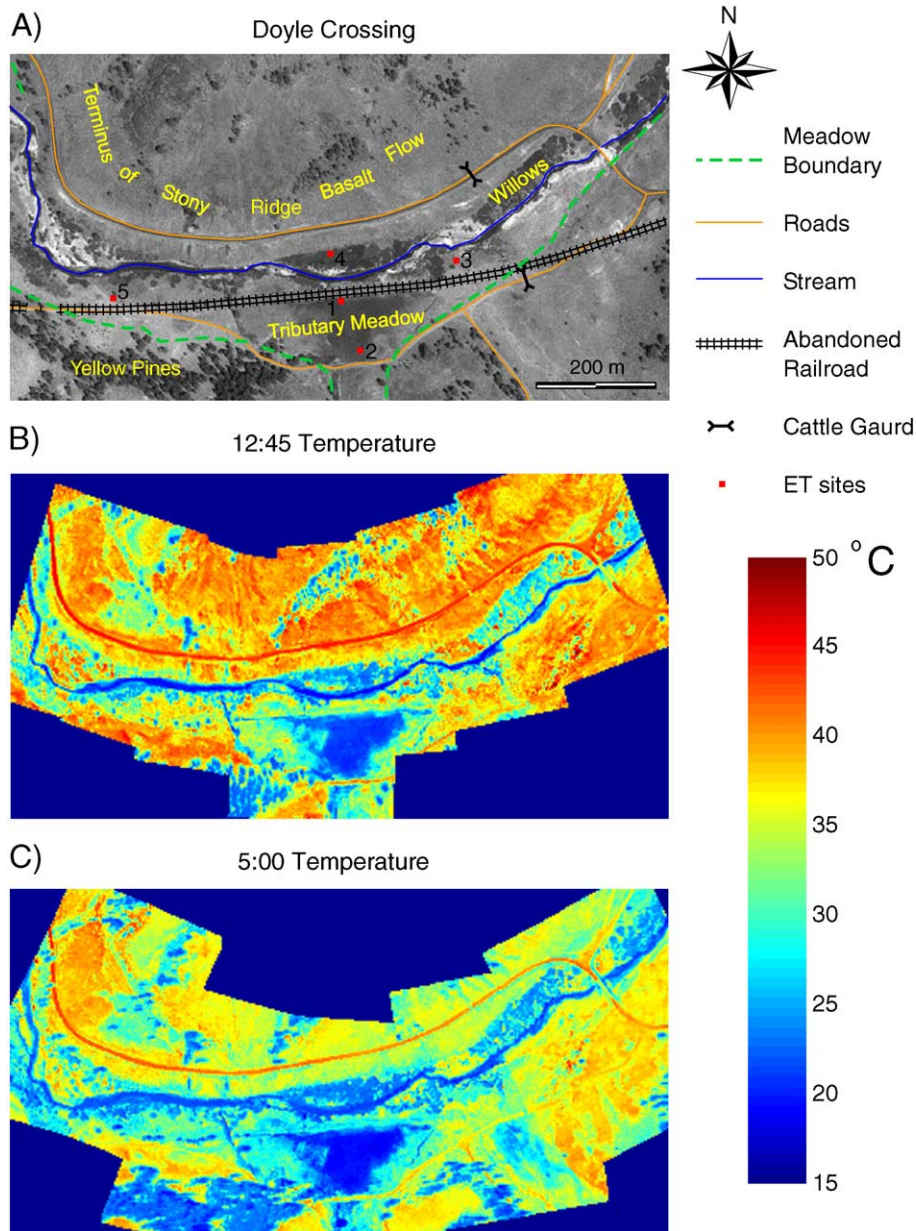


Fig. 3. A) Map of features at Doyle Crossing overlain on USGS digital orthorectified quadrangle. B) Registered surface temperature map at 12:45 PM. C) Registered surface temperature map at 5:00 PM.

At the four meadows described earlier, frames selected from each flight were georeferenced to 1-m digital orthorectified quadrangles (DOQ).⁴ Image-to-image registration was accomplished by selecting 8–12 notable landmarks per image such as edges of specific trees, identifiable stream features, intersections of bridges, fence lines, roads, etc. Several images were mosaiced together using the nearest neighbor method of subsampling to a standard grid having 1 m pixel size. Fig. 3 is an example of the digital

orthoquad that was used as a base map at Doyle Crossing and the 12:45 and 5:00 pm temperature maps. Because the high resolution of the imagery matched that of the DOQ, accurate and consistent registration was possible for both flights.

3.1.2. Weather station

A weather station⁵ was installed at an elevation of 1736 m in Big Flat (Fig. 1) meadow which is approximately 5 km

⁴ DOQ's produced by the United States Geological Survey and distributed by the California Spatial Information Library.

⁵ Hobo weather station manufactured by Onset Computer Corp (Pocasset, MA).

northeast of Doyle Crossing and 5 km northwest of Coyote Flat. Big Flat is a restored meadow and the weather station is located in a region of healthy meadow vegetation. Air temperature (T_{air}) was recorded by two thermistors at a height of 2 m. Wind speed (u), humidity (h), shortwave solar radiation (R_S), and precipitation (P) were also measured at this height. Soil temperature (T_{soil}) was recorded at 5 and 10 cm depths. Every 15 min we logged instantaneous measurements of T_{air} , T_{soil} , and h , plus average values of u and R_S . Data were compared to a California Department of Water Resources weather station (Station ID DOY) located on a rocky hillslope approximately 1 km to the northeast of Doyle Crossing at an elevation of 1728 m.

3.1.3. Plot scale ET measurements

Plot scale (1 m²) measurements of ET were made using a steady-state porometer⁶ to measure stomatal response. Following McDermitt (1990) we measured the stomatal resistance with the porometer and then calculated the transpiration rate using in situ values of air temperature, leaf temperature, relative humidity, and calculated boundary layer resistance; we did not use the vapor flux measured by the porometer as a transpiration rate. Here, the standardized procedure documented by the Food and Agriculture Organization of the United Nations guidelines was used to apply the Penman–Monteith equation based on the measured stomatal resistance that was used to estimate the surface resistance of the canopy as a whole (Allen et al., 1998). Meteorological data from the weather station were used to calculate ET at 15 min intervals and estimates during daylight hours were integrated to obtain daily vegetative consumptive water use. A total of 69 measurements were used to estimate ET at 5 representative plots within the study area.

3.2. Theory

3.2.1. Heat budget

The four major components of the 1-D surface heat budget Eq. (1) are the latent heat flux (L), the sensible heat flux (H), the net radiation (R_N), and the ground heat flux (G),

$$A = R_N - G = L + H. \quad (1)$$

The available energy (A) is partitioned between the sensible and latent heat fluxes. The latent heat flux is the quantity of interest in this study. It is defined as the latent heat of vaporization (λ) multiplied by the ET_{inst} rate and represents the heat removed by the process of evapotranspiration. The sensible heat flux (H), on the other hand, represents the combined processes of heat conduction and

turbulent convection. It is driven by the gradient between the air temperature at a specified height and the surface temperature as shown in Eq. (2),

$$H = \frac{\rho_a C_p (T_{\text{surface}} - T_{\text{air}})}{r_a + r_{\text{excess}}} \quad (2)$$

where ρ_a and C_p are the density and heat capacity of the air, T_{surface} is the surface temperature, T_{air} is the air temperature at the standard height, r_a is aerodynamic resistance, and r_{excess} is the excess resistance that is encountered for heat transfer compared to momentum transfer (Norman & Becker, 1995). It is worthwhile to note that the excess resistance in Eq. (2) is functionally equivalent to considering a difference between a radiometric surface temperature and the aerodynamic temperature when the difference between these quantities and the air temperature are proportional (Chehbouni et al., 1997; Watts et al., 1997). Hall et al. (1992), Kustas et al. (1989), Moran et al. (1994), and Stewart et al. (1994) have all used the extra resistance term as a means of accounting for the difference between the aerodynamic temperature and the radiometric temperature. Several studies have shown that use of a constant value for the excess resistance produces acceptable results (Burke & Stewart, 1997), however, other parameterizations for this term that are dependent on leaf area index (Chehbouni et al., 1996, 1997) or surface temperature are available (Lhomme et al., 2000). In future applications of ETMA, an alternate formulation of this term may be found to be more appropriate.

If we assume the spatial derivatives of the available energy, air temperature, excess resistance, and the aerodynamic resistance to heat transfer are zero, then both the latent and sensible heat fluxes are linearly related to the surface temperature. Here we introduce two temperatures T_{latent} and T_{sensible} that are defined as the surface temperature at which the available heat flux is partitioned completely to the latent and sensible heat fluxes, respectively. T_{latent} is necessarily the temperature at which $H=0$; therefore, from Eq. (2), $T_{\text{latent}}=T_{\text{air}}$. Similarly, as shown in Eq. (3), T_{sensible} is determined by solving Eq. (2) for the condition when $H=A$ given by Eq. (1),

$$T_{\text{sensible}} = \frac{A(r_a + r_{\text{excess}})}{\rho_a C_p} + T_{\text{air}} \quad (3)$$

Then the ET_{inst} rate can be determined using Eq. (4) as shown below:

$$\text{ET}_{\text{inst}} = \left[A \frac{(T_{\text{sensible}} - T_{\text{surface}})}{(T_{\text{sensible}} - T_{\text{latent}})} \right] / \lambda \quad (4)$$

Suleiman and Crago (2004) presented a similar approach for partitioning of the energy budget but framed it in terms of dimensionless temperature theory and used a different parameterization of the roughness length. They compared hourly ET estimates from stationary radiometers with those from adjacent eddy covariance stations and found correla-

⁶ Li-Cor 1600 steady-state porometer (Lincoln, NE).

tion coefficients ranging from 0.78 and 0.94 even though the footprint of these estimates differ significantly. Where our approach diverges conceptually from that of Suleiman and Crago (2004) is in using this theory to map ET_{inst} and extrapolate it to daily values using the Penman–Montieth and Jarvis–Stewart equations to model the diurnal pattern of ET at each pixel location.

3.2.2. Penman–Montieth equation

The daily pattern of ET can be modeled, as detailed in Allen et al. (1998), using the Penman–Montieth Equation, Eq. (5),

$$ET_{\text{inst}} = \frac{(R_n - G)(\Delta) + \rho_a c_p \left(\frac{e_s - e}{r_a} \right)}{\lambda \left[\Delta + \gamma \left(1 + \frac{r_s}{r_a} \right) \right]} \quad (5)$$

where Δ represents the slope of the vapor pressure temperature relationship, ρ_a is the density of the air, c_p is the heat capacity of the air, r_s is the surface resistance, r_a is the aerodynamic resistance, e_s is the saturated vapor pressure, e is the actual vapor pressure, and γ is the psychrometric constant.

The aerodynamic resistance can be calculated with Eq. (6),

$$r_a = \frac{\ln \left[\frac{z_m - d}{z_{om}} \right] \ln \left[\frac{z_h - d}{z_{oh}} \right]}{k^2 u} \quad (6)$$

where z_m and z_h are the height of the wind and humidity measurements, d is the zero plane displacement height, z_{om} and z_{oh} are the roughness lengths for momentum and heat transfer, u is the measured wind velocity, and k is von Karman's constant. As recommended by Allen et al. (1998), vegetation height (h_{veg}) can be used to estimate the roughness lengths and the zero plane displacement heights as follows in Eqs. (7)–(9),

$$z_{om} = 0.123 h_{\text{veg}} \quad (7)$$

$$z_{oh} = 0.1 z_{om} \quad (8)$$

$$d = \frac{2}{3} h_{\text{veg}} \quad (9)$$

3.2.3. Jarvis–Stewart model of surface conductance

The surface conductance ($g_s = 1/r_s$) may vary diurnally and can be modeled with Eq. (10), a Jarvis–Stewart type formulation:

$$g_s = g_{\text{max}} g(R_s) g(q) g(T_{\text{air}}) g(\delta\theta) \quad (10)$$

where g_{max} is the maximum surface conductance and $g(R)$, $g(q)$, $g(T_{\text{air}})$, and $g(\delta\theta)$ are the functional dependencies of solar radiation, specific humidity deficit, temperature, and soil moisture deficit, respectively, on surface conductance

(Jarvis, 1976; Stewart, 1988). Stewart (1988) wrote $g(R_s)$ and $g(\delta)$ as follows in Eqs. (11) and (12), respectively,

$$g(R_s) = \frac{(1 + c/1000)(R_s)}{R_s + c} \quad (11)$$

$$g(\delta) = 1 - a(\delta) \quad (12)$$

where c and a are empirical coefficients. Since temperature has a small effect on stomatal response (Lhomme & Elguero, 1999) and water availability is not believed to change significantly over the course of the day in our study, $g(T_{\text{air}})$ and $g(\delta\theta)$ are neglected by setting them equal to unity.

3.3. ET mapping algorithm (ETMA)

The ET mapping algorithm (ETMA) outlined here (Fig. 4) was developed for applications that require high spatial resolution ET maps at local scales where conditions are semi-uniform. ETMA requires local meteorological and ground heat flux data from a representative weather station and remotely sensed surface temperatures (FLIR) at one or more times during a day (Table 1). The first step of ETMA is to determine the available energy, T_{latent} and T_{sensible} . The available energy is the net radiation minus the ground heat flux as shown in Eq. (1). In Eq. (13), the ground heat flux is calculated using the measured gradient in soil temperature and an estimate of the thermal conductivity of the soil as shown below:

$$G \approx -k_{\text{soil}} \frac{\partial T_{\text{soil}}}{\partial z} \quad (13)$$

where k_{soil} is the thermal conductivity of the soil at the current moisture content.

The net radiation is calculated as recommended by Shuttleworth (1993) using the measured solar radiation, vapor pressure, air temperature, and Eqs. (14)–(16):

$$R_n = R_{\text{nl}} + R_{\text{ns}} \quad (14)$$

$$R_{\text{ns}} = (1 - \alpha) R_s \quad (15)$$

$$R_{\text{nl}} = - \left(.9 \frac{n}{N} + 0.1 \right) (0.34 - 0.14\sqrt{e}) \sigma T_{\text{air}}^4 \quad (16)$$

where R_{ns} is the net shortwave radiation, R_{nl} is the net longwave radiation, α is the albedo, n/N is the sunshine hour ratio, σ is the Stefan–Boltzmann constant, and e is the vapor pressure in kilopascal. Alternatively, the net radiation could be measured with a net radiometer if such data were available. Since ETMA is intended for application at the local scale, the net radiation is assumed to be spatially constant. Spatially variable components may be estimated from narrow band reflectance data if these bands are collected during the remote sensing campaign (Daughtry et al., 1990; Moran et al., 1989).

T_{latent} is taken to be the average air temperature for the half hour prior to and including the remote sensing flights. Although Eq. (1) and Eq. (2) relate to instantaneous fluxes, this time period was selected because the observed surface

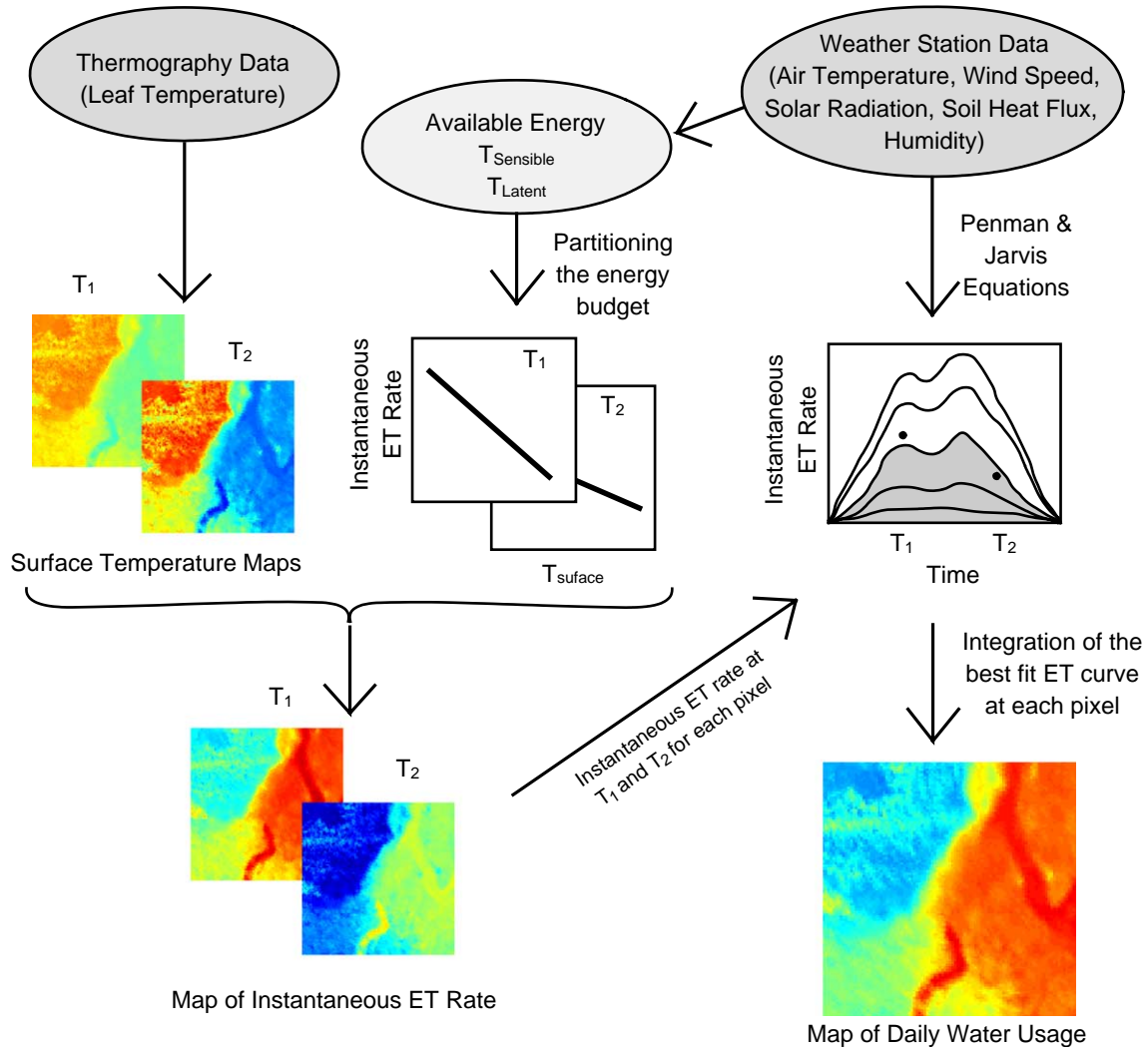


Fig. 4. Flow diagram of the ET mapping algorithm (ETMA). Two data sources, namely thermography and weather station data, including the soil heat flux, are required to produce maps of surface temperature and relationships between ET_{inst} rate and observed surface temperature, respectively. When the ET_{inst} vs. T relationships are applied to the temperature maps, maps of ET_{inst} are produced. The Penman–Montieth and Jarvis–Stewart equations, driven by the weather-station data, are used to model the daily temporal pattern of ET. Using ET_{inst} rates from co-located pixels, the best fit pattern of ET is determined by varying the surface resistance. The map of ET_{day} is created by integrating the best fit daily ET pattern at each pixel.

temperatures (soil and vegetation) do not respond immediately to changing meteorological conditions but instead have some memory of recent conditions that helps to buffer the effect of high frequency changes. This distinction is not important when conditions vary in a slow and smooth manner but may be important if these variables are changing quickly over a wide range. In Eq. (2), $T_{sensible}$ was substituted for

$T_{surface}$ and H was substituted for A to solve for $T_{sensible}$. In order to determine the value of $T_{sensible}$, values of r_a and r_{excess} are calculated using the mean air temperature and wind speed measured during the same period for which T_{latent} was determined. Eqs. (6)–(9) in addition to the stability corrections from Businger–Dyer formulations (Businger, 1988; Zhang & Lemeur, 1995) are used to determine the aerodynamic resistance. The value of r_{excess} is determined with Eq. (17) as given in Norman and Becker (1995),

$$r_{excess} = \frac{1}{0.4U^*} \ln\left(\frac{z_{om}}{z_{oh}}\right) \tag{17}$$

where U^* is the friction velocity defined by Eq. (18),

$$\frac{u}{U^*} = \frac{\ln\left(\frac{z_m - d}{z_{om}}\right)}{k} \tag{18}$$

and u is the wind velocity.

Table 1

Data requirements for ETMA

Air temperature (at reference height)
Humidity (at reference height)
Wind speed (at reference height)
Solar radiation
Ground heat flux
Stewart–Jarvis parameter estimates
Vegetation height (mean or spatially distributed)
High-resolution, remotely sensed (FLIR) surface temperature maps

Once the values of available energy, T_{latent} , and T_{sensible} , have been determined for each flight, then one transfer function relating surface temperature to ET_{inst} rate is found for each flight with Eq. (4). The next step of ETMA is to apply these transfer functions to their respective maps of temperature to obtain maps of ET_{inst} . Because the observed surface temperature may occasionally be greater than T_{sensible} , the predicted rate may be less than zero in this case. The few pixels with negative ET rates that occurred (e.g., roads) were assumed zero since condensation at land surface was deemed implausible during this time period. From these maps of ET_{inst} , estimates from co-located pixels are extracted so the daily pattern of ET can be modeled at each pixel location. The daily pattern of ET is described by Eq. (5) where the surface resistance varies over the course of the day as described by Eqs. (10)–(12). Values of the empirical coefficients, $c=400$ and $a=24$, were given by Stewart and Gay (1989) for the case of the Konza Prairie in Kansas; these values were also found to be reasonable for this site based on the observed pattern of diurnal variation in porometry data. The best fit diurnal pattern of ET was selected by minimizing the squared error, varying only g_{max} in Eq. (10). The integrated daily water consumption (ET_{day}) was then determined by integrating the best fit diurnal pattern of ET over the day of interest.

4. Results

4.1. ETMA performance

4.1.1. Step-by-step ETMA results at Doyle Crossing

Fig. 3A shows a map of Doyle Crossing overlain on the digital orthoquad that was used for registration of the six thermal images that make up the 12:45 PM temperature map (Fig. 3B) and the five thermal images that make up the 5:00 PM temperature map (Fig. 3C). In these mosaics, no discontinuities appear at the boundaries of individual images. It is clear that many of the same thermal patterns appear in both temperature maps; however, the surface temperatures are generally warmer at 12:45 PM than 5:00 PM by an average of 3.6 °C. The tributary meadow appears as a cool anomaly (20–25 °C) as do the willows and the near-stream region. The sagebrush-dominated portions of the riparian zone and the sparsely vegetated terminus of Stony Ridge appear 15–25 °C warmer than the tributary meadow.

The relationships between observed surface temperature and ET_{inst} rate for both flights are shown in Fig. 5. These relationships were created assuming a plant height of 0.3 m, which is reasonable for both the meadow and sagebrush scrub vegetation communities. One point on this graph of surface temperature versus ET_{inst} is $(T_{\text{sensible}}, 0)$ which is known from the definition of T_{sensible} which is the temperature at which the latent heat flux (i.e., ET) equals zero. Similarly, the definition of T_{latent} provides a second point on

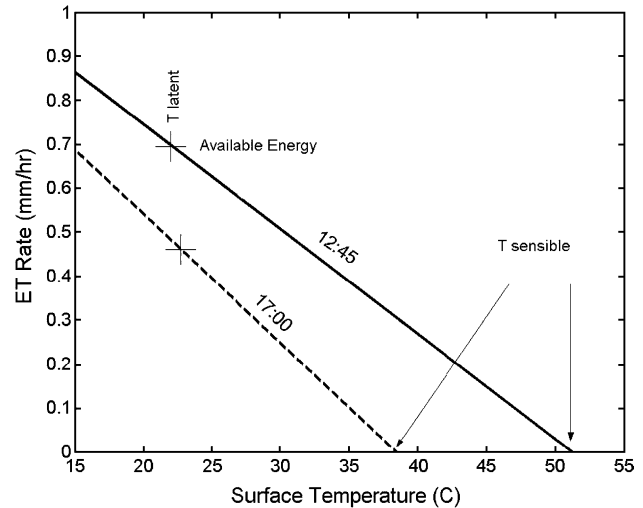


Fig. 5. Calculated relationship between surface temperature and ET_{inst} rate. Calculation of T_{latent} and T_{sensible} as described in the text is used to determine this relationship.

this graph at the location $(T_{\text{latent}}, A/\lambda)$. From Eq. (2), this relationship, which is expressed in Eq. (4), is expected to be linear assuming uniform air temperature, aerodynamic resistance (plant height and wind speed), and excess resistance. These assumptions have caused major stumbling blocks associated with regional application of direct methods such as the simplified relationship; however, on the local scale, accuracy of these methods may be 10–15% (see Caurault et al. (2003) for further discussion).

It is important to note that ETMA is designed for local-scale application where land cover, meteorological conditions, and topography are relatively uniform. For instance, in our case both the degraded and restored meadow vegetation have similar canopy height ($\sim 0.3\text{m}$), however, if the canopy height had varied in the region of interest, separate relationships between ET and surface temperature would have been needed for each land-cover type to account for the effect on the aerodynamic resistance in Eqs. (6)–(9). Similarly, if not applied at a local scale with a known air temperature, the assumption that $dT_{\text{air}}/dx=0$ may be violated (Caurault et al., 1998; Gash, 1987) and even 1 °C error in $T_{\text{surface}} - T_{\text{air}}$ may cause significant error in estimation of the sensible heat flux particularly for tall vegetation at high wind speeds (Norman et al., 1995). In addition, it is not only the spatial uniformity, but also the temporal continuity, that must be considered. Eqs. (1) and (2) are taken as instantaneous rates of heat transfer, however we apply meteorological parameters representative of a half-hour period to drive these equations. If T_{air} is variable over time, the derived relationship between ET_{inst} and T_{surface} would shift to the left or right through time as can be seen by considering the definitions of T_{sensible} and T_{latent} . In our study this temporal variability was not a major concern; for example, the recorded air temperature at 12:30, 12:45, and 1:00 was 22.06, 21.94, and 21.92 °C, respectively. Averaging of extreme variations in wind speed can potentially

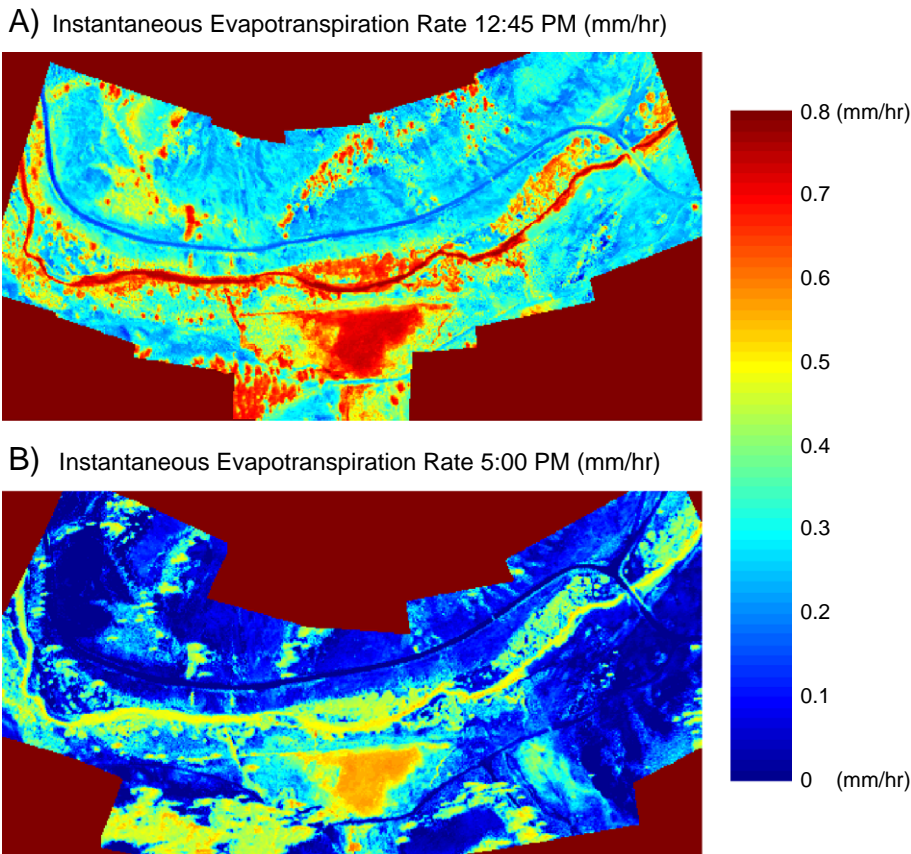


Fig. 6. Doyle Crossing. A) ET_{inst} map at 12:45 PM. B) ET_{inst} map at 5:00 PM.

introduce error in estimation of $T_{sensible}$ (and also ET) through the effect of wind speed in the aerodynamic resistance term in Eq. (6). However, in our study, the peak wind gust was never more than a factor of two greater than the mean wind speed.

These relationships are then applied to the temperature maps to create the maps of ET_{inst} rates shown in Fig. 6. Here we see the same patterns as in the temperature maps with cool anomalies representing regions of high ET. The ET rates are typically greater at 12:45 PM than 5:00 PM even though the temperatures at 12:45 were higher. This is because higher available energy and the higher value of $T_{sensible}$ during the 12:45 flight resulted in ET_{inst} rates that were greater than those from the 5:00 flight for all values of surface temperature that were observed (Fig. 5).

Fig. 7 shows the ET_{inst} rates (mapped) at the pixels located at Sites 1, 3, and 4 along with the best fit model of the daily ET pattern (modeled). Sites 1 and 3 show good fit, however, at Site 4, the modeled pattern and the estimated ET_{inst} rates differ by 0.08 mm/h. The reasons for this difference will be discussed later. However, in this diurnal pattern, a dip occurs between 13:00 and 14:45 because of thin, high-level clouds that developed during this time. The ETMA algorithm provides a non-linear means of accurately estimating daily values of ET by integrating the pattern of ET using Eqs. (5) and (10) under these conditions. Using

either clear skies assumptions or the assumption of a constant evaporative fraction would not produce the same results when scaling instantaneous values to daily values. A map of minimum surface resistance that was determined to provide the most accurate match between the modeled pattern of ET and the estimated ET_{inst} rates is shown in

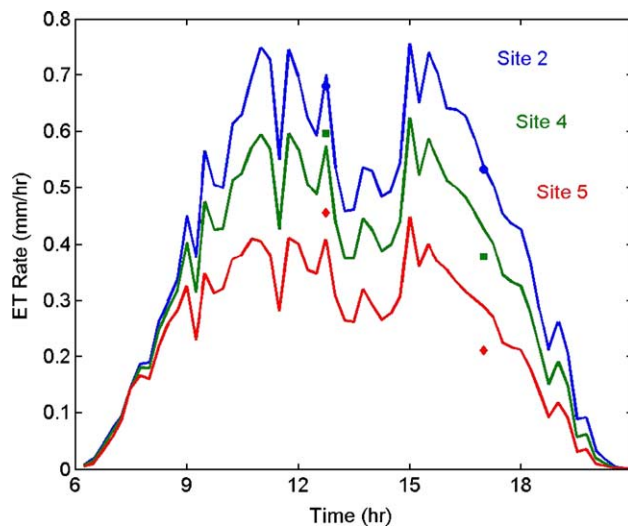


Fig. 7. Best fit temporal pattern of ET modeled with the Penman–Montieth equation and conditioned to the two instantaneous estimates at three sites.

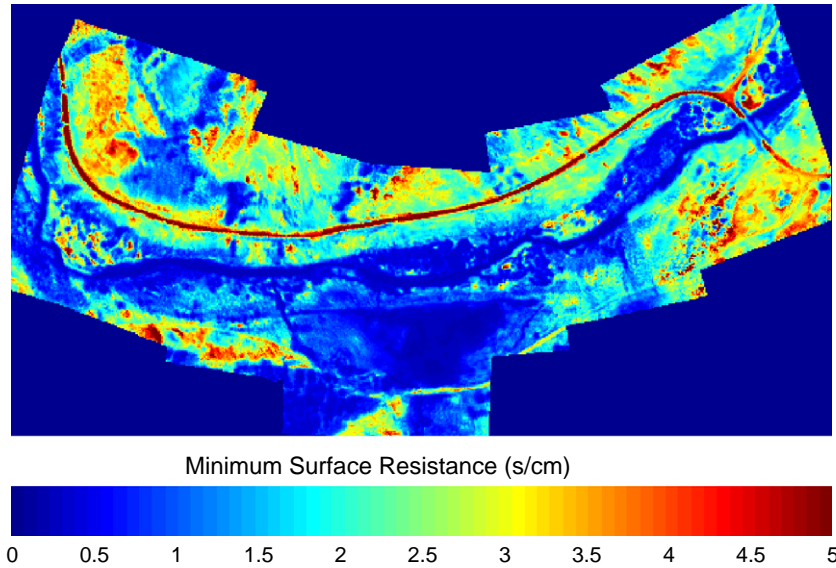


Fig. 8. Map of the minimum surface resistance at Doyle Crossing.

Fig. 8. The areas of low surface resistance correlate to regions of lush vegetation. Fig. 9 shows ET_{day} , which is the integral of this best fit ET pattern (Fig. 7). Generalizing, the meadow vegetation at Doyle Crossing consumed 5.0–7.0 mm/day of water, the willows consumed 4.5–6.0 mm/day, the degraded riparian areas consumed 1.0–3.5 mm/day, and the sparse hillslopes consumed less than 2.5 mm/day. Fig. 10 is a map of the root mean square mismatch between the mapped ET_{inst} rates (Fig. 6) and the modeled ET at each pixel location. The spatial distribution and causes for this mismatch will be discussed later.

4.1.2. Validation of results

The ETMA model assumes that all parameters measured or estimated from the weather station (importantly the net

radiation, the soil heat flux, the air temperature, wind speed, and the humidity) are spatially uniform. We believe that at the site scale, when the area of interest is nearly uniform and topographically smooth, this assumption will be acceptable. To test this assumption, we compared the weather data collected at Big Flat with that near Doyle Crossing, with the anticipation that since the Doyle Crossing station is situated on a rocky outcrop on Stony Ridge, it would represent the warmest, driest, and windiest locations in the watershed, whereas the Big Flat station would represent the opposite extremes. At the Doyle Crossing site, air temperature (recorded hourly) was found to be consistently warmer from the hours of 9:00 AM to 7:00 PM by an average of 1.0 °C, an error that is relatively small compared to the observed 30° range of surface temperatures. Similarly, humidity

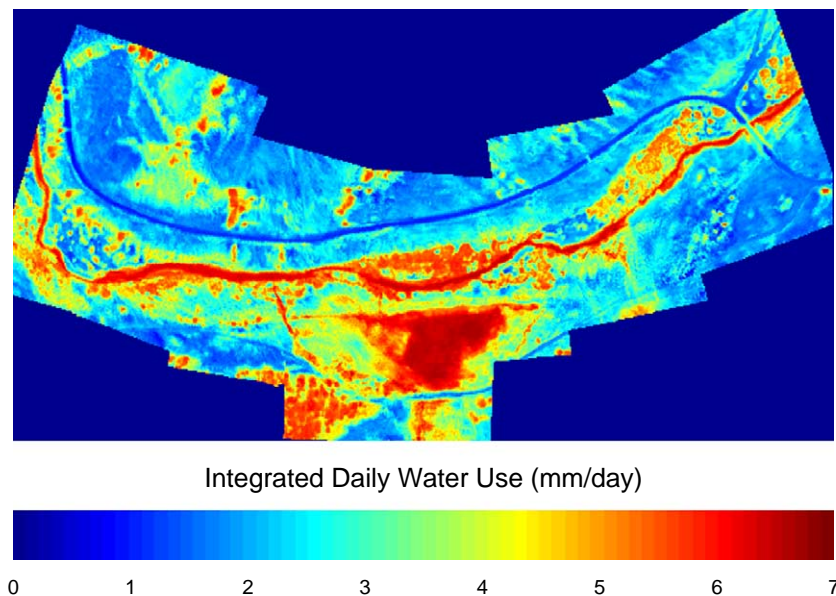


Fig. 9. Map of the integrated daily evapotranspirative water use (ET_{day}) at Doyle Crossing.

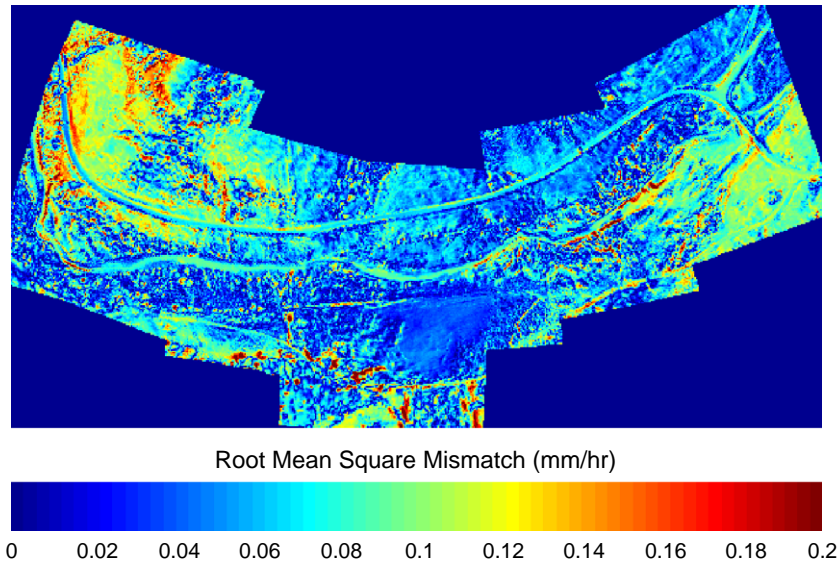


Fig. 10. Map of the root mean square mismatch at Doyle Crossing. Mismatch is focused on the hillslopes with a west-facing aspect.

(recorded hourly) was found to be consistently lower from the hours of 9:00 am to 7:00 pm by an average of 4% at the Doyle Crossing weather station, which represents less than 5% error in the vapor pressure deficit since the average humidity was 15–20%. Wind speed did not differ significantly. This comparison demonstrates that the spatial heterogeneity of the meteorological data is negligible in the context of this study and those parameters measured at the Big Flat station are in fact representative of the entire study area. While the ground heat flux may likely be spatially variable, this component of the heat budget typically had a magnitude less than 10% of the available energy. Because the ground heat flux is such a small percentage of the available energy, even large errors in the soil heat flux (e.g., 50%) will only have a small impact on ET estimates (>5% of the potential ET rate).

The results obtained by application of ETMA were compared with three other estimates of ET. First, a pan evaporation measurement was collected adjacent to the weather station between 11:30 AM on 6/01/04 and 9:00 AM on 6/05/04. During this 3.83-day period, an average pan evaporation rate of 7.0 mm/day was recorded. This corresponds to a potential ET rate of 5.60–5.95 mm/day using a pan coefficient of 0.80–0.85 (Allen et al., 1998). An independent estimate of the potential ET rate was determined to be 5.04 mm/day from the observed meteorological data using the standardized procedure from Allen et al. (1998). This range of potential ET rates (5.04–5.95 mm/day) is within the range of ETMA estimates (5.0–6.5 mm/day) that was observed for healthy meadow vegetation, which is believed to be transpiring at a rate similar to the potential rate. Second, in situ measurements of stomatal conductance that were collected with the porometer were used in Eq. (3) to estimate daily ET at five sites within Doyle Crossing. These estimates are plotted against those obtained with ETMA in Fig. 11 and show a mean

difference of -0.05 mm/day, a mean absolute difference of 0.33 mm/day, and a mean absolute percentage difference of 7.6%. A third estimate of groundwater use by vegetation was obtained by applying the White method (White, 1932) to recorded diurnal fluctuations (~ 11 cm) in the water table at a piezometer near Site 1 at Doyle Crossing. This estimate of groundwater use is assumed equal to the total ET because the water table is within 20 cm of the land surface. Procedures given by Loheide et al. (2005) were used and the resulting estimate was 6.8 mm/day for the day. Both the pan and White method estimates suggest that ETMA accurately predicts the near potential ET rates observed in areas with healthy meadow vegetation. Furthermore, Fig. 11 indicates that the ETMA accurately estimates rates throughout the observed range and bounded by the potential ET rate.

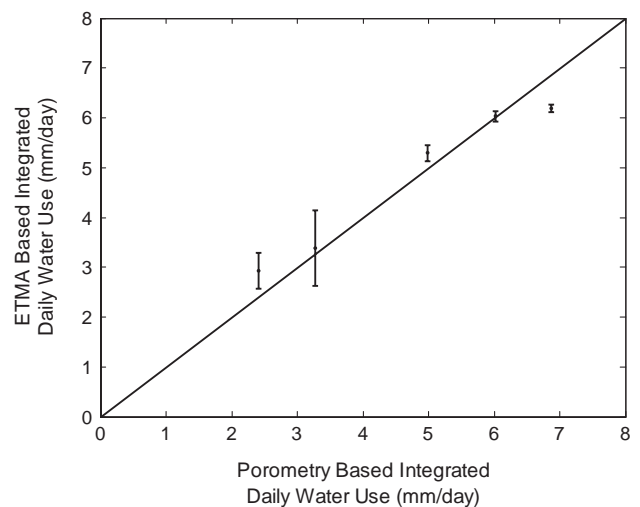


Fig. 11. Porometer data estimates versus ETMA estimates of ET_{day} . The error bars are an indication of spatial variability and are calculated as the standard deviation of ET_{day} for the pixels within 2 m of the groundtruth location.

The results from the other meadows will be reserved for the next section, however the performance of ETMA at these sites will be discussed here. The mean root mean square mismatch between the mapped ET_{inst} rates and the modeled ET at each pixel location and standard deviation (std) of this quantity for the entire images at Alkali Flat, Artray Meadow, Coyote Flat, and Doyle Crossing are 0.086 (std=0.029), 0.096 (std=0.054), 0.029 (std=0.026), and 0.069 (std=0.038) mm/h. If we remove all values on the hillslopes from the analysis, the mismatch is smaller for the meadows only and the values are 0.076 (std=0.022), 0.076 (std=0.039), 0.028 (std=0.025), and 0.060 (std=0.038)

mm/h, respectively. These mismatches represent a relative error of 15%, 17%, 10%, and 16%, respectively. This mismatch is a measure of model error and can be divided into three types. An example of the first and most severe error can be seen on the western side of the terminus of the Stony Ridge Basalt Flow in Fig. 10. Topographically, this region of the ridge has a west to southwest aspect such that during the 5:00 flight this area was exposed to incident radiation at a much higher angle than the low light angle that reached the flat meadow environments. Thus, this hillslope and others with a west- or southwest-facing aspect were exposed to more intense incoming radiation during the 5:00 flight. This

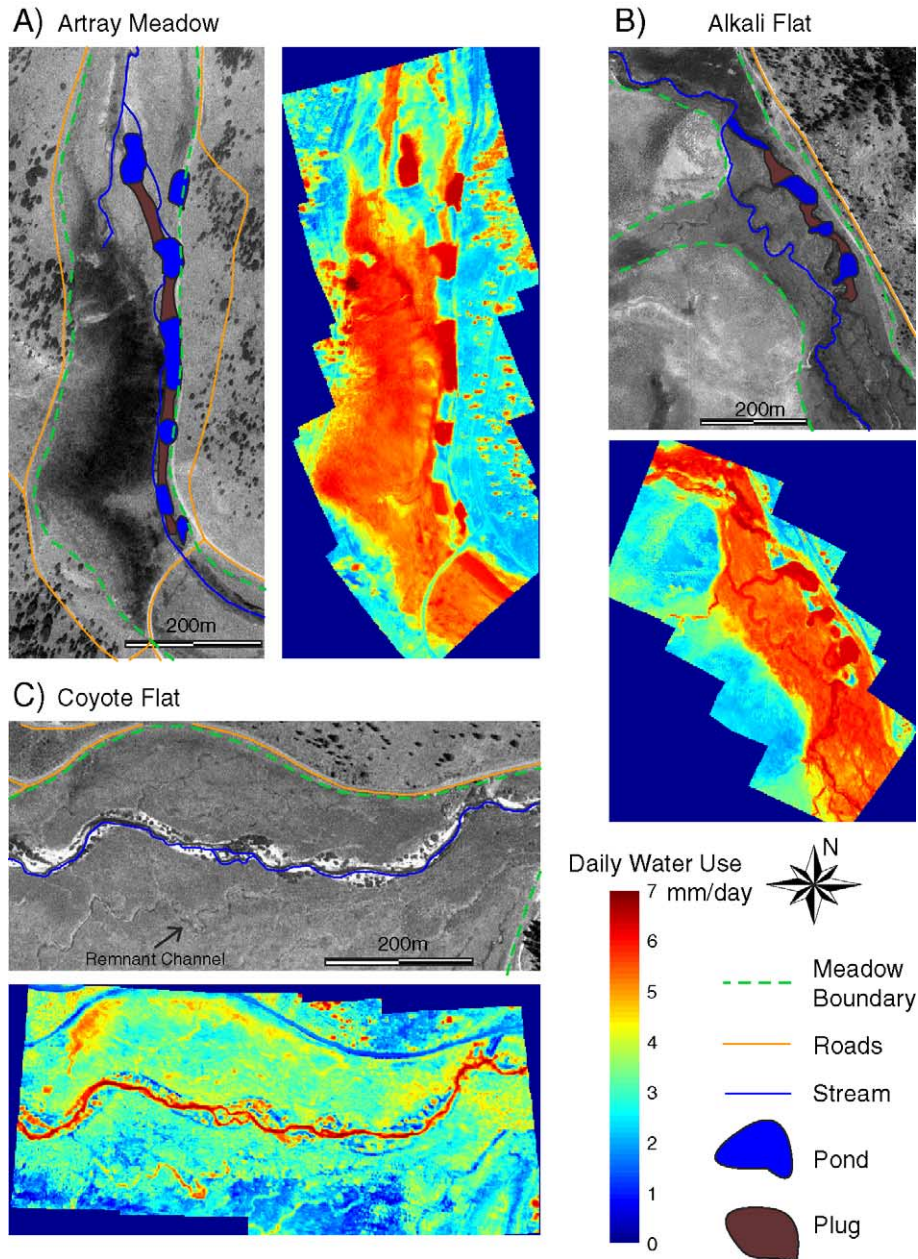


Fig. 12. Paired site and ET_{day} maps for A) Artray Meadow, B) Alkali Flat, and C) Coyote Flat. Artray Meadow and Alkali Flat are examples of restored meadows whereas Coyote Flat and Doyle Crossing in Fig. 9 are degraded meadow systems. Higher ET demand is seen in the riparian areas of the restored meadows.

violates the model assumption of spatially uniform available energy. Since the available energy is higher than assumed on these hillslopes, T_{sensible} is also underestimated and both of these factors contribute to underestimation of the ET_{inst} rate for all observed surface temperatures in Fig. 3C. Since the ET rates during the 5:00 flight are underestimated, it is impossible to obtain a good fit to the daily ET pattern in the hillslope regions. The result is that the integrated daily vegetative water consumption for these pixels may be underestimated by as much as 1.2 mm/day or 18% of the potential rate. Fortunately, in this study, these regions where estimates are known to be biased are on the hillslopes but are not biased in the flat meadows that are of primary interest. To minimize this error, a geometric correction based on topographic slope and sun angle could be applied to estimate the available energy in this region.

The second source of error occurs in the shadows of the large conifer trees. Since the position of the shadow moves between the two flights, the cool footprint of the tree moves. The assumptions of the one-dimensional heat budget with a uniform available energy are again violated. In this case, the available energy is much lower in the shade of the trees and the estimate of T_{sensible} is too high, which results in overestimation of the ET_{inst} rates for these pixels. This leads to a biased (over-) estimation of the integrated daily water consumption in the shade of the trees. This source of error is again not significant in the meadow systems.

The third source of mismatch between the observed ET_{inst} rates and the modeled diurnal ET pattern can be seen in the degraded meadow systems and near any sharp contacts between different surfaces (i.e., road–vegetation contacts). This mismatch results from slight (<2 m) errors in the registration of the thermal imagery, causing co-located pixels to be spatially mismatched. The degraded meadows are heterogeneous on scales greater than 1 m; 1 m² plot might be dominated by a clump of sagebrush, whereas neighboring plots might contain dryland grasses, holdout sedges and rushes or high percentages of bare ground. Thus when pixels from the two flights are not properly aligned with each other, a modeled daily ET pattern is fit for two pixels that are not precisely co-located. This only becomes a source of mismatch when neighboring pixels contain different vegetation types. The effect of this error is to produce a nearly unbiased estimate that is smoother than the true integrated daily ET.

4.2. Daily water consumption in degraded and restored meadows

The motivation for developing ETMA was to determine whether there are significant and quantifiable differences between the daily evapotranspirative water use in degraded and restored meadows. In addition to Fig. 9, which is an ET_{day} map of Doyle Crossing (degraded), Fig. 12 shows ET_{day} for three additional meadows—Artray Meadow (restored), Alkali Flat (restored), and Coyote Flat (degraded).

The results are clear; evapotranspiration is greater in the restored meadows than in those that are degraded. We quantified this observation in Fig. 13A and B, which show the normalized frequency distributions ET_{day} for the degraded meadows and restored meadows, respectively. These distributions were constructed by first counting the number of pixels within the meadow boundaries shown in Figs. 3 and 12 that have values that fall within bins of 0.125 mm/day width. This count was then normalized by the total number of pixels in the meadow and the width of the bin. The most notable difference between the restored and degraded distributions is the peak of the distribution in the restored cases located from 5.0 to 6.5 mm/day, which corresponds to the healthy meadow vegetation. The distribution from Coyote Flat represents a completely degraded system and shows a peak between 1.5 and 4.0 mm/day. The fact that the vegetation within the meadow system at Doyle Crossing is a mix between the degraded system along the main stem of Last Chance Creek and the healthy tributary meadow can be seen in the broad and relatively uniform distribution spanning

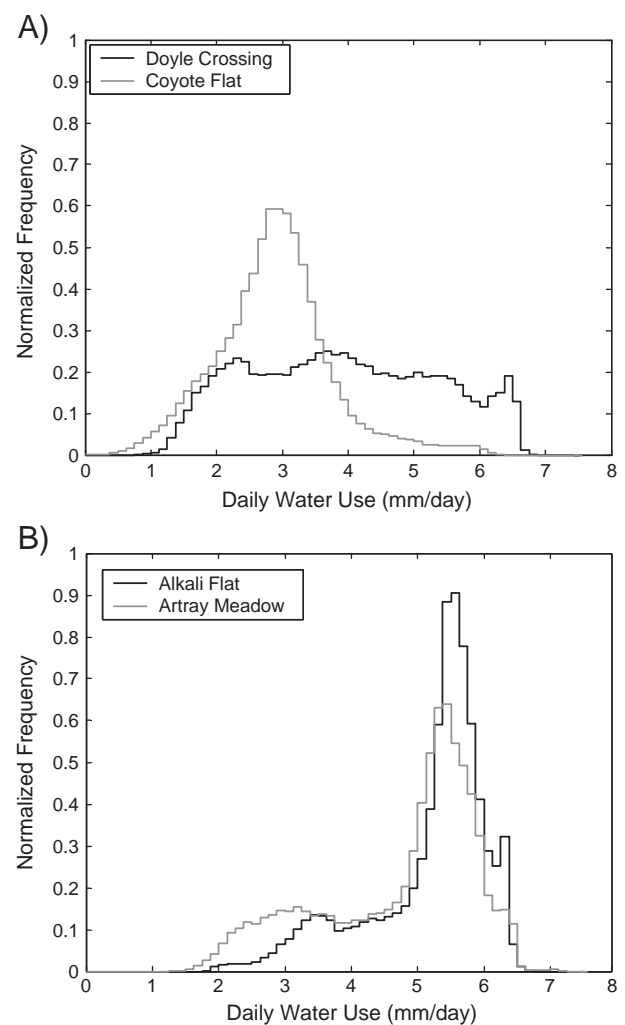


Fig. 13. Normalized frequency distributions of ET_{day} for pixels in A) Doyle Crossing and Coyote Flat degraded meadows and B) Alkali Flat and Artray restored meadows.

1.5–6.5 mm/day (Fig. 13A). The univariate mean and standard deviation for Alkali Flat, Artray Meadow, Coyote Flat, and Doyle Crossing are 5.16 ± 0.91 , 4.75 ± 1.17 , 2.88 ± 0.89 , and 3.92 ± 1.42 mm/day. While the hillslopes are not of primary interest in this study, the daily evapotranspirative consumption (ET_{day}) in these regions was typically less than 3 mm/day and may represent bare surface evaporation in some portions of the hillslopes.

In addition to the gross differences in water consumption, many subtle features are noteworthy in both restored and degraded cases. In the Doyle Crossing meadow (Fig. 9), it is clear that the abandoned railroad bed has played a role in the degradation of the main channel and in the preservation of the tributary meadow. The railroad bed is raised by approximately 0.5 m relative to the surrounding flood plain. This barrier presumably confined floodwaters to the north side of the railroad bed, resulting in higher stream flow velocity, increased shear stress, increased erosive capability, and, ultimately, stream incision of 2–3 m. At the same time, the railroad bed has prevented incision from propagating into the tributary meadow, therefore preserving a high water table and native meadow vegetation. In the meadow at Doyle Crossing, it is also possible to differentiate among slightly different land-use practices. The two cattle guards shown on the map in Fig. 3A, which also appear on the thermal imagery in Fig. 3B and C, are connected by a straight fence. A subtle difference can be seen in the surface temperature (Fig. 3) and ET_{day} (Fig. 9) on either side of the fence at Doyle Crossing. This difference in ET is likely due to differences in the timing of grazing in these two adjacent grazing allotments.

In both the restored meadows, Artray Meadow and Alkali Flat, the boundary between the flat meadow flood plain and the upland vegetation is striking on the maps of integrated daily consumption (Fig. 12). This implies a sharp boundary between vegetation types that may be caused by a relatively slight increase in elevation of perhaps 1–2 m that seems to prohibit the roots of the meadow vegetation from accessing the groundwater. In both of these meadows, it is also clear that the vegetation on the plugs is transpiring at a much lower rate than the other vegetation. Artray Meadow, which was restored during 2002, was seeded only by reserving topsoil from the excavation of the ponds and spreading it on the surface of the plugs. Alkali Flat was restored a year later and native seeds were gathered and then spread on the plugs to supplement the seed bank from the spreading of the topsoil. While the plug vegetation in neither of the restored meadows seemed to be thriving at the time of this study, June 3, 2004, we observed in the field that the vegetation on the plugs in Alkali Flat appeared to strengthen later that year. ETMA will be used to track the evolution of the restored meadows to see whether the harvesting and spreading of native seeds help to establish vegetation on the plugs.

At Artray Meadow, the northern third of the meadow system shows lower integrated water consumption. This is the downstream end of the project area, below which

restoration could not be completed because of the archaeological significance of that area. Thus, the streamflow is diverted into the incised channel. It appears that this lower channel is draining that portion of the meadow and healthy meadow vegetation has not yet been re-established.

Coyote Flat is the most severely degraded meadow, but even at this site two areas indicate that the succession to a sagebrush scrub community is not complete. The road in the northern portion of the scene (Fig. 12C) follows a contour just above the break in slope between the hillslope and the flat meadow. Below this break in topographic slope is a likely location for groundwater discharge into the meadow system. Furthermore, this region of the meadow is distant from the incised channel, which has caused lowering of the water table. The slightly higher ET rates observed in this region indicate greater groundwater availability near the root zone, presumably from one of the two above-mentioned mechanisms. Similarly, an abandoned remnant channel south of the incised channel is situated approximately 1–1.5 m below the meadow surface. While there is typically no standing water in this channel, it does retain soil moisture and is nearer to the water table making it a more hospitable environment for meadow vegetation. This remnant channel appears as an area of slightly higher ET. In addition, a small flood plain has started to develop adjacent to the incised channel. Much of this flood plain is covered with loose sand; however, willows and some patches of vegetation have taken hold and appear as small patches of higher ET.

5. Conclusions

An evapotranspiration mapping algorithm, ETMA, is developed and demonstrated as a new tool that is potentially valuable in disciplines such as hydroecology, precision agriculture, forestry, and rangeland sciences where high-resolution maps (~1 m) of evapotranspiration could be used to monitor, track, and understand land-use practices and climatic or environmental changes affecting vegetation. The methodology uses commercially available equipment that can be affordably rented, making this type of high-resolution thermal remote sensing readily available. With the relatively simple procedures outlined here, users can obtain maps of daily evapotranspirative water consumption (ET_{day}) in areas that are nearly uniform and topographically smooth on any day when thermal remote sensing data are collected. While the current version of ETMA is intended only for local-scale application with uniform conditions, extension to situations with spatially variable land cover or environmental conditions is straightforward. If the spatial pattern in parameters such as aerodynamic resistance, excess resistance, air temperature, or available energy is known or can be estimated from other data sources, a simple modification to ETMA would be to determine a separate relationship between ET_{inst} and T_{surface} at each pixel that

considers these spatially variable parameters. ETMA is not limited by clear sky or constant evaporative fraction assumptions (Zhang & Lemeur, 1995) and site-specific empirical calibrations need not be made. In this study, our results suggest that estimates of ET_{day} within the meadow environment are accurate to within approximately 10% of the potential rate or an absolute difference of 0.7 mm/day. Under some conditions, larger errors may result; for example, the approach is less accurate in westward-facing, low-ET hillslopes, where the error may be twice as large due to underestimation of the available energy in this region. Our future work includes developing methods to temporally scale ET maps obtained for specific days to estimate ET demand over the entire growing season.

Significant differences were observed between integrated evapotranspirative water consumption in the paired degraded and restored meadows along Last Chance Creek in the Feather River Watershed, CA. Through the processes of transpiration and evaporation, the sagebrush scrub vegetation community in the degraded portions of the system consumed 1.5–4 mm/day, whereas the wet meadow vegetation community that is dominated by sedges and rushes had an ET demand of 5–6.5 mm/day. Thus, the wet meadow-vegetation environment uses approximately twice the water used in the degraded meadows.

The spatial resolution of the ET maps obtained here are at the necessary scales to study the hydroecology of meadow restoration. The patterns observed here revealed that restoration had largely succeeded in raising the water table and re-establishing the pre-degradation ecohydrology. The work also revealed less successful re-vegetation on the plugs and in the downstream end of the Artray Meadow project. This information will be used by the FRCRM in designing future restoration projects and the FRCRM anticipates using these techniques for future monitoring. The ETMA methodology provides a tool for long-term monitoring of these restoration projects to determine whether they have reached a steady state, whether unanticipated effects may cause the projects to fail in the long run, and whether the intended return of meadow vegetation is still progressing.

6. Notation

A	Available energy [$E/L^2/t$]
a	Empirical coefficient [–]
C_p	Heat capacity of the air [$E/M/T$]
c	Empirical coefficient [–]
d	Zero plane displacement height [L]
ET_{day}	Integrated daily evapotranspiration [L/T]
ET_{inst}	Instantaneous evapotranspiration rate [L/T]
e_s	Saturated vapor pressure [$M/L/t^2$]
e	Actual vapor pressure [$M/L/t^2$]
G	Ground heat flux [$E/L^2/t$]
g_s	Surface conductance [L/t]
g_{max}	Maximum surface conductance [L/t]

$g(q)$	Functional dependency of specific humidity deficit on surface conductance [–]
$g(R_s)$	Functional dependency of solar radiation on surface conductance [–]
$g(T_{\text{air}})$	Functional dependency of temperature on surface conductance [–]
$g(\delta\theta)$	Functional dependency of soil moisture deficit on surface conductance [–]
H	Sensible heat flux [$E/L^2/t$]
h	Humidity [–]
h_{veg}	Vegetation height [L]
k	von Karman's constant [–]
k_{soil}	Thermal conductivity of the soil at the current moisture content [$E/L/t/T$]
L	Latent heat flux [$E/L^2/t$]
N	Maximum duration of sunshine [t]
n	Actual duration of sunshine [t]
R_{ns}	Net shortwave radiation [$E/L^2/t$]
R_{nl}	Net longwave radiation [$E/L^2/t$]
R_s	Shortwave solar radiation [$E/L^2/t$]
R_N	Net radiation [$E/L^2/t$]
r_a	Aerodynamic resistance [t/L]
r_{excess}	Excess resistance [t/L]
r_s	Surface resistance [t/L]
P	Precipitation [L]
T_{air}	Air temperature [T]
T_{latent}	Value of T_{surface} at which A is partitioned completely to the latent heat flux [T]
T_{sensible}	Value of T_{surface} at which A is partitioned completely to the sensible heat flux [T]
T_{soil}	Soil temperature [T]
T_{surface}	Surface temperature [T]
U^*	The friction velocity [L/t]
u	Wind speed [L/t]
z_h	Height of the humidity measurements [L]
z_m	Height of the wind speed measurements [L]
z_{om}	Roughness length for momentum transfer [L]
z_{oh}	Roughness length for heat transfer [L]
α	Albedo [–]
γ	Psychrometric constant [$M/L/T/t^2$]
Δ	Slope of the vapor pressure temperature relationship [$M/L/T/t^2$]
λ	Latent heat of vaporization [E/M]
ρ_a	Density of the air [M/L^3]
σ	Stefan–Boltzmann constant [$E/t/T/m^2$]

Acknowledgments

This material is based upon work supported by the National Science Foundation under Grant No. EAR-0337393. Any opinions, findings, and conclusions or recommendations expressed in this material are those of the authors and do not necessarily reflect the views of the National Science Foundation. Adam Abeles, Celeste Avila, Brian Ebel, Chris Heppner, Nick Martin, Ben Mirus, and

Mike Ronayne helped with collection of data in the field. Professor Christopher Fields allowed us to borrow his Li-Cor porometer. We are grateful to Terry Benoit, Leslie Mink, and Jim Wilcox who are staff at the FRCRM and who helped, particularly in the early phases of this work, to familiarize us with the sites and the restoration work they are doing and provided support and encouragement throughout this study. We acknowledge the Plumas National Forest Service for access to the sites and interest in the project. We are also grateful for comments from two anonymous reviewers that helped to improve this manuscript.

References

- Allen, R. G., Pereira, L. S., Raies, D., & Smith, M. (1998). Crop evapotranspiration: Guidelines for computing crop water requirements. *FAO Irrigation and Drainage Paper*, 56, 300.
- Bastiaanssen, W. G. M., Ahmad, M., & Chemin, Y. (2002). Satellite surveillance of evaporative depletion across the Indus Basin. *Water Resources Research*, 38(12), 9-1–9-9.
- Bastiaanssen, W. G. M., Menenti, M., Feddes, R. A., & Holtslag, A. A. M. (1998). A remote sensing surface energy balance algorithm for land (SEBAL): 1. Formulation. *Journal of Hydrology*, 212–213, 198–212.
- Boegh, E., Soegaard, H., & Thomsen, A. (2002). Evaluating evapotranspiration rates and surface conditions using Landsat TM to estimate atmospheric resistance and surface resistance. *Remote Sensing of Environment*, 79, 329–343.
- Boulet, G., Chehbouni, A., & Braud, I. (1998). Mosaic versus dual source approaches for modeling the surface energy balance of a semi-arid land. *American Meteorological Society, Special Symposium on Hydrology, Phoenix Arizona* (pp. 1–7).
- Brutsaert, W., & Sugita, M. (1992). Application of self-preservation in the diurnal evolution of the surface energy budget to determine daily evaporation. *Journal of Geophysical Research*, 97(D17), 18377–18382.
- Burke, E. J., & Stewart, J. B. (1997). Test of a sensible heat flux–radiometric surface temperature relationship for HAPEX-SAHEL. *Boundary-Layer Meteorology*, 84(2), 329–337.
- Businger, J. A. (1988). A note on the Businger–Dyer profiles. *Boundary-Layer Meteorology*, 42, 145–151.
- Carlson, T. N., Capehart, W. J., & Gillies, R. R. (1995). A new look at the simplified method for remote-sensing of daily evapotranspiration. *Remote Sensing of Environment*, 54(2), 161–167.
- Caurault, D., Seguin, B., & Olios, A. (2003). Review to estimate evapotranspiration from remote sensing data: Some examples from the simplified relationship to the use of mesoscale atmospheric models. *ICID workshop on remote sensing of ET for large regions, 17th September, 2003*.
- Courault, D., Clastre, P., Cauchi, P., & Delecolle, R. (1998). Analysis of spatial variability of air temperature at regional scale using remote sensing data and a SVAT model. *Proceed. of 1st Inter. Conf. on Geospatial Information in Agriculture and Forestry, vol. II* (pp. 149–156).
- Chebouni, A., Lo Seen, D., Njoku, E., & Monteny, B. (1996). Examination of the difference between radiative and aerodynamic surface temperatures over sparsely vegetated surfaces. *Remote Sensing of Environment*, 58, 177–186.
- Chebouni, A., Lo Seen, D., Njoku, E., Olios, A., Monteny, B., & Kerr, Y. H. (1997). Estimation of sensible heat flux over sparsely vegetated surfaces. *Journal of Hydrology*, 188–189, 855–868.
- Daughtry, C., Kustas, W. P., Moran, M. S., Pinter, J. P. J., Jackson, R. D., & Brown, P. W., et al. (1990). Spectral estimates of net radiation and soil heat flux. *Remote Sensing of Environment*, 32, 111–124.
- Feather River Coordinated Resource Management Group (1997). Fact Sheet #1: The Feather River Coordinated Management Group. Feather River Coordinated Management Group.
- Gash, J. H. C. (1987). An analytical framework for extrapolation evaporation measurements by remote sensing surface temperature. *International Journal of Remote Sensing*, 8(8), 1245–1249.
- Goodrich, D. C., Scott, R., Qi, J., Goff, B., Unkrich, C. L., & Moran, M. S., et al. (2000). Seasonal estimates of riparian evapotranspiration using remote and in situ measurements. *Agricultural and Forest Meteorology*, 105(1–3), 281–309.
- Granger, R. J. (2000). Satellite-derived estimates of evapotranspiration in the Gediz basin. *Journal of Hydrology*, 229(1–2), 70–76.
- Hall, F. G., Huemmrich, K. F., Geotz, S. J., Sellers, P. J., & Nickerson, J. E. (1992). Satellite remote sensing of surface energy balance: Successes, failures, and unresolved issues in FIFE. *Journal of Geophysical Research*, 97(D17), 19061–19090.
- Jackson, R. D., Hatfield, J. L., Reginato, R. J., Idso, S. B., & Pinter, J. P. J. (1983). Estimates of daily evapotranspiration from one time of day measurements. *Agricultural Water Management*, 7, 351–362.
- Jackson, R. D., Reginato, R. J., & Idso, S. B. (1977). Wheat canopy temperatures: A practical tool for evaluating water requirements. *Water Resources Research*, 13(3), 651–656.
- Jacob, F., Olioson, A., Gu, X. F., Su, Z., & Seguin, B. (2002). Mapping surface fluxes using airborne visible, near infrared, thermal infrared remote sensing data and a spatialized surface energy balance model. *Agronomie*, 22, 669–680.
- Jarvis, P. G. (1976). The interpretation of leaf water potential and stomatal conductance found in canopies in the field. *Philosophical Transactions of the Royal Society of London*, 273, 593–610.
- Jenson, J. R. (2000). *Remote sensing of the environment: An earth resource perspective* (p. 251). Upper Saddle River: Prentice Hall.
- Kite, G. W., & Droogers, P. (2000). Comparing evapotranspiration estimates from satellites, hydrological models and field data. *Journal of Hydrology*, 229, 3–18.
- Kustas, W. P., Choudhury, B. J., Moran, M. S., Reginato, R. J., Jackson, R. D., & Gay, L. W., et al. (1989). Determination of sensible heat flux over sparse canopy using thermal infrared data. *Agricultural and Forest Meteorology*, 44, 197–216.
- Kustas, W. P., Humes, K. S., Norman, J. M., & Moran, M. S. (1996). Single- and dual-source modeling of surface energy fluxes with radiometric surface temperature. *Journal of Applied Meteorology*, 35, 110–121.
- Kustas, W. P., & Norman, J. M. (1996). Use of remote sensing for evapotranspiration monitoring over land surfaces. *Hydrological Sciences*, 41(4), 495–516.
- Kustas, W. P., & Norman, J. M. (2000). Evaluating the effects of subpixel heterogeneity on pixel average fluxes. *Remote Sensing of Environment*, 74(3), 327–342.
- Lhomme, J. P., & Chehbouni, A. (1999). Comments on dual-source vegetation–atmosphere transfer models. *Agricultural and Forest Meteorology*, 94, 269–273.
- Lhomme, J. P., Chehbouni, A., & Monteny, B. (2000). Sensible heat flux–radiometric surface temperature relationship over sparse vegetation: Parameterizing b-1. *Boundary-Layer Meteorology*, 97, 431–457.
- Lhomme, J. P., & Elguero, E. (1999). Examination of evaporative fraction diurnal behaviour using a soil–vegetation model coupled with a mixed-layer model. *Hydrology and Earth System Sciences*, 3(2), 259–270.
- Lindquist, D. S., & Wilcox, J. (2000). *New concepts for meadow restoration in the northern Sierra Nevada*. Feather River Coordinated Resource Management Group.
- Loheide, S. P. II, Butler, J. J. Jr., & Gorelick, S. M. (2005). Estimation of groundwater consumption by phreatophytes using diurnal water table fluctuations: A saturated–unsaturated flow assessment. *Water Resources Research*, 41, W07030. doi:10.1029/2005WR003942.
- McDermitt, D. K. (1990). Sources of error in the estimation of stomatal conductance and transpiration from porometer data. *HortScience*, 25(12), 1538–1548.

- Micheli, E. R., & Kirchner, J. W. (2002). Effects of wet meadow riparian vegetation on streambank erosion: 1. Remote sensing measurements of streambank migration and erodibility. *Earth Surface Processes and Landforms*, 27, 627–639.
- Moran, M. S. (2003). Thermal infrared measurements as an indicator of plant ecosystem health. In D. A. Quattrochi, II, & J. C. Luvall (Eds.), *Thermal infrared measurements as an indicator of plant ecosystem health*. Philadelphia, PA: Taylor and Francis.
- Moran, M. S., Clark, T. R., Kustas, W. P., Wetz, M., & Amer, S. A. (1994). Evaluation of hydrologic parameters in a semiarid rangeland using remotely sensed spectral data. *Water Resources Research*, 30(5), 1287–1297.
- Moran, M. S., Jackson, R. D., Raymond, L. H., Gay, L. W., & Slater, P. N. (1989). Mapping surface energy balance components by combining LANDSAT Thematic Mapper and ground-based meteorological data. *Remote Sensing of Environment*, 30, 77–87.
- Murray, B. R., Zeppel, M. J. B., Hose, G. C., & Eamus, D. (2003). Groundwater-dependent ecosystems in Australia: It's more than just water for rivers. *Ecological Management and Restoration*, 4, S53–S59.
- Nagler, P. L., Cleverly, J., Glenn, E., Lampkin, D., Huete, A., & Wan, Z. (2005). Predicting riparian evapotranspiration from MODIS vegetation indices and meteorological data. *Remote Sensing of Environment*, 94(1), 17–30.
- Nieuwenhuis, G., Schmidt, E., & Tunnissen, H. (1985). Estimation of regional evapotranspiration of arable crops from thermal infrared images. *International Journal of Remote Sensing*, 6, 1319–1334.
- Norman, J. M., Anderson, M. C., Kustas, W. P., French, A. N., Mecikalski, J., Tom, R., Diak, G. R., Schmugge, T. J., & Tanner, B. C. W. (2003). Remote sensing of surface energy fluxes at 10⁰–1 m pixel resolutions. *Water Resources Research*, 39(8), 9-1:9-18.
- Norman, J. M., & Becker, F. (1995). Terminology in thermal infrared remote sensing of natural surfaces. *Agricultural and Forest Meteorology*, 77, 153–166.
- Norman, J. M., Kustas, W. P., & Humes, K. S. (1995). Sources approach for estimating soil and vegetation energy fluxes in observations of directional radiometric surface temperature. *Agricultural and Forest Meteorology*, 77, 263–293.
- Northeast Midwest Institute (2005). <http://www.nemw.org/calfed.htm>, <http://www.nemw.org/calfed.htm>
- Pietroniro, A., & Prowse, T. D. (2002). Applications of remote sensing in hydrology. *Hydrological Processes*, 16, 1537–1541.
- Plumas Corporation (2004). *Final report: Last chance watershed restoration project* (p. 55).
- Qiu, G. Y., Miyamoto, K., Sase, S., Gao, Y., Shi, P. J., & Yano, T. (2002). Comparison of the three-temperature model and conventional models for estimating transpiration. *Jarq-Japan Agricultural Research Quarterly*, 36(2), 73–82.
- Ratliff, R. (1985). Meadows in the Sierra Nevada of California: State of knowledge. USDA General Technical Report PSW-84.
- Rosgen, D. (1996). *Applied river morphology*. Pagosa Springs, CO: Wildland Hydrology.
- Schultz, G. A., & Engman, E. T. (2000). *Remote sensing in hydrology and water management*. New York: Springer.
- Seguin, B., & Itier, B. (1983). Using midday surface temperature to estimate daily evaporation from satellite thermal IR data. *International Journal of Remote Sensing*, 4(2), 371–383.
- Shuttleworth, W. J. (1993). Evaporation. In D. R. Maidment (Ed.), *Evaporation*. New York: McGraw Hill.
- Stewart, J. B. (1988). Modelling surface conductance of pine forest. *Agricultural and Forest Meteorology*, 43, 19–37.
- Stewart, J. B., & Gay, L. W. (1989). Preliminary modelling of transpiration from the FIFE site in Kansas. *Agricultural and Forest Meteorology*, 48, 305–315.
- Stewart, J. B., Kustas, W. P., Humes, K. S., Nichols, W. D., Moran, M. S., & de Bruin, H. A. R. (1994). Sensible heat flux–radiometric surface temperature relationship for 8 semi-arid areas. *Journal of Applied Meteorology*, 33, 1110–1117.
- Suleiman, A., & Crago, R. (2004). Hourly and daytime evapotranspiration from grassland using radiometric surface temperature. *Agronomy Journal*, 96, 384–390.
- Water Science and Technology Board, & Board on Environmental Studies and Toxicology (2002). *Riparian areas: Functions and strategies for management*. Washington, DC: National Academy Press.
- Watts, C. J., Chehbouni, A., Rodriguez, J. C., Kerr, Y. H., Hartogensis, O., & de Bruin, H. A. R. (1997). Comparison of sensible heat flux estimates using AVHRR with scintillometer measurements over semi-arid grassland in northwest Mexico. *Agricultural and Forest Meteorology*, 105(1), 81–89.
- White, W. N. (1932). *A method of estimating ground-water supplies based on discharge by plants and evaporation from soil: Results of investigations in Escalante Valley, Utah*. United States Department of the Interior.
- Zhang, L., & Lemeur, R. (1995). Evaluation of daily evapotranspiration estimates from instantaneous measurements. *Agricultural and Forest Meteorology*, 74(1–2), 139–154.